A MULTIGRID LU FACTORIZATION SCHEME FOR THE THIN-LAYER NAVIER-STOKES EQUATIONS

Timo Siikonen, Jaakko Hoffren and Seppo Laine

Laboratory of Aerodynamics
Helsinki University of Technology
02150 Espoo, Finland

Abstract

A finite-volume-based numerical method for the solution of the Euler and thin-layer Navier-Stokes equations is presented. The convective part of the fluxes is solved using a flux-vector splitting method and the diffusive part using central differences. The equations are integrated in time with an approximately factored implicit scheme. Convergence is accelerated by applying a multigrid technique. Results are presented for inviscid and viscous flows over an NACA 0012 airfoil and for three-dimensional laminar and turbulent flows over a body of revolution at high angles of attack.

1. INTRODUCTION

In recent years upwind difference methods have become popular in solving both inviscid and viscous flow problems. Upwind methods are intrinsically dissipative and require no additional dissipative terms. Due to the intrinsic dissipation, computational algorithms based on the upwind differences are usually more robust than the algorithms based on the central differences. The drawback of the upwind methods is the strong dissipation inside shear layers and in the case of low Mach number inviscic flows.

There are many ways to employ the upwind concept for the flow equations. These include the flux-vector splitting method of Van Leer[1] and the flux-difference splitting of Roe.[2] In the present paper we use the method of Van Leer for inviscid and viscous flows. The method is applied in a cell-centred finite-volume form. On the cell boundaries the convective part of the fluxes is split in a locally one-dimensional fashion. The thin-layer approximation is performed for the viscous terms.

The flow equations are integrated in time using an approximately factored bidiagonal scheme.[3] The effect of the viscous terms is taken into account by modifying the diagonal eigenvalue matrices arising from the linearization of the convective fluxes. The integration method is approximative and the resulting maximum CFL-number is of the order of one. The convergence is accelerated using a multigrid method.

Computational results in a two-dimensional case are presented for inviscid and viscous transonic flow over an NACA 0012 airfoil. The turbulent viscosity is calculated using the Baldwin-Lomax turbulence model. Three-dimensional results are shown for a laminar and turbulent flow over a body of revolution at high angles of attack.

2. GOVERNING EQUATIONS

2.1 Differential Form

The Navier-Stokes equations can be written in a conservative form using Cartesian coordinates as

$$\frac{\partial U}{\partial t}+\frac{\partial F(U)}{\partial x}+\frac{\partial G(U)}{\partial y}+\frac{\partial H(U)}{\partial z}=0 \qquad (1)$$

where $U=(\rho \quad \rho u \quad \rho v \quad \rho w \quad e)^T$

$$F=\begin{pmatrix} \rho u \\ \rho u^2+p-\tau_{xx} \\ \rho uv-\tau_{xy} \\ \rho uw-\tau_{xz} \\ u(p+e-\tau_{xx})-\tau_{xy}v-\tau_{xz}w+q_x \end{pmatrix} \qquad (2)$$

$$G=\begin{pmatrix} \rho v \\ \rho vu-\tau_{xy} \\ \rho v^2+p-\tau_{yy} \\ \rho vw-\tau_{yz} \\ v(p+e-\tau_{yy})-\tau_{xy}u-\tau_{yz}w+q_y \end{pmatrix} \qquad (3)$$

$$H=\begin{pmatrix} \rho w \\ \rho wu-\tau_{xz} \\ \rho wv-\tau_{yz} \\ \rho w^2+p-\tau_{zz} \\ w(p+e-\tau_{zz})-\tau_{xz}u-\tau_{yz}v+q_z \end{pmatrix} \qquad (4)$$

and

$$\tau_{ij}=\mu\left(\frac{\partial u_i}{\partial x_j}+\frac{\partial u_j}{\partial x_i}\right)-\frac{2}{3}\mu\frac{\partial u_k}{\partial x_k}\delta_{ij} \qquad (5)$$

$$q_i=-k\frac{\partial T}{\partial x_i} \qquad (6)$$

Here U is the vector of conservative variables, ρ the density; the velocity components are u, v and w, μ is the viscosity coefficient, p is the pressure, e the total internal energy, k the thermal conductivity, and T the temperature. The definition of the second coefficient of viscosity: $\lambda=-2/3\mu$, has been taken into account in the formula of the viscous stress tensor τ_{ij}.

The pressure is calculated from

$$p=(\gamma-1)\left(e-\rho\frac{u^2+v^2+w^2}{2}\right) \qquad (7)$$

where γ is the specific heat ratio.

For the solution, the flow equations are scaled as follows:

$$x^*=\frac{x}{L} \qquad t^*=\frac{t}{(L/c_\infty)} \qquad u^*=\frac{u}{c_\infty} \qquad \mu^*=\frac{\mu}{\mu_\infty}$$

$$\rho^* = \frac{\rho}{\rho_\infty} \qquad p^* = \frac{p}{\rho_\infty c_\infty^2} \qquad T^* = \frac{T}{T_\infty} \qquad e^* = \frac{e}{\rho_\infty c_\infty^2} \tag{8}$$

Here the subscript ∞ refers to free stream conditions and c is the velocity of sound. This transformation retains the form of the Euler equations, whereas the dimensionless stress tensor is

$$\tau_{ij} = \frac{Ma_\infty}{Re_\infty}\mu[(\frac{\partial u_i}{\partial x_j} + \frac{\partial u_j}{\partial x_i}) - \frac{2}{3}\frac{\partial u_k}{\partial x_k}\delta_{ij}] \tag{9}$$

Here and in the following, the superscripts have been dropped for simplicity.

The heat flux is calculated from

$$q_i = -k\frac{\partial T}{\partial x_i} = -\frac{c_p\mu}{Pr}\frac{\partial T}{\partial x_i} \tag{10}$$

After scaling we obtain

$$q_i = -\frac{Ma_\infty\mu}{(\gamma-1)PrRe_\infty}\frac{\partial T}{\partial x_i} \tag{11}$$

In the following, a constant Prandtl number $Pr = 0.72$ is assumed.

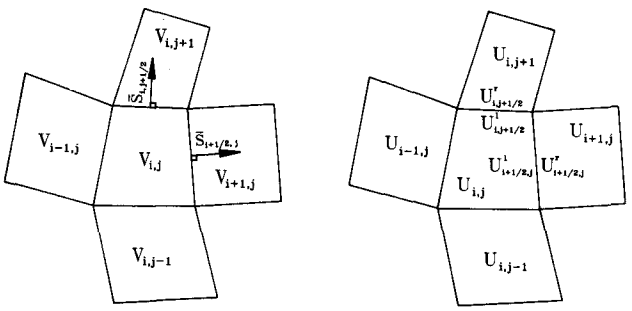

a) Geometry b) Location of variables

Fig. 1. Computational grid used in the flux-vector splitting method.

2.2 Finite-Volume Form

The flow equations have an integral form

$$\frac{\partial}{\partial t}\int_V U dV + \int_S \vec{F}(U)\cdot d\vec{S} = 0 \tag{12}$$

where V represents the cell volume and S the cell face area. The cell face area can be expressed using the Cartesian base vectors

$$\vec{S} = S_x\vec{i} + S_y\vec{j} + S_z\vec{k} \tag{13}$$

The corresponding unit vector is

$$\vec{n} = n_x\vec{i} + n_y\vec{j} + n_z\vec{k} = \frac{S_x}{S}\vec{i} + \frac{S_y}{S}\vec{j} + \frac{S_z}{S}\vec{k} \tag{14}$$

Performing the integrations of Eq.(12) for a computational cell i shown in Fig. 1a yields

$$V_i\frac{dU_i}{dt} = \sum_{faces} -S\hat{F} \tag{15}$$

where the sum is taken over the faces of the computational cell and

$$\hat{F} = n_xF + n_yG + n_zH \tag{16}$$

For clarity, the viscous part of the u-momentum equation is rewritten

$$\hat{F}_{2,v} = -\frac{Ma_\infty\mu}{Re_\infty}[\frac{2}{3}(2\frac{\partial u}{\partial x} - \frac{\partial v}{\partial y} - \frac{\partial w}{\partial z})n_x + (\frac{\partial u}{\partial y} + \frac{\partial v}{\partial x})n_y + (\frac{\partial w}{\partial x} + \frac{\partial u}{\partial z})n_z] \tag{17}$$

Similar equations are obtained for the viscous parts of the v- and w-momentum equations, $\hat{F}_{3,v}$ and $\hat{F}_{4,v}$. The corresponding part of the energy flux is written as

$$\hat{F}_{5,v} = u\hat{F}_{2,v} + v\hat{F}_{3,v} + w\hat{F}_{4,v} - \frac{Ma_\infty\mu}{(\gamma-1)PrRe_\infty}(\frac{\partial T}{\partial x}n_x + \frac{\partial T}{\partial y}n_y + \frac{\partial T}{\partial z}n_z) \tag{18}$$

3. SPATIAL DISCRETIZATION

3.1 Calculation of the Fluxes

The calculation of the convective parts of the fluxes is based on the rotational invariance of the Euler equations. On a cell surface the convective flux is calculated from

$$\hat{F} = T^{-1}[F^+(TU^l) + F^-(TU^r)] \tag{19}$$

Here F^+ and F^- are Van Leer's split fluxes[1], U^l and U^r are the values of the solution vector evaluated on the cell surface and

$$T = \begin{pmatrix} 1 & 0 & 0 & 0 & 0 \\ 0 & n_x & n_y & n_z & 0 \\ 0 & -n_y & n_x & 0 & 0 \\ 0 & -n_z & 0 & n_x & 0 \\ 0 & 0 & & 0 & 1 \end{pmatrix} \tag{20}$$

is a rotation matrix. After multiplying by the rotation matrix the fluxes have the same functional form as in the case of the Cartesian coordinates and can be split similarly. In a two-dimensional case this procedure has no drawbacks. However, in a three-dimensional case the matrix T is singular if $n_x = 0$. This can be avoided by choosing another rotation matrix. The requirement for the rotation matrix is that the third and the fourth lines of T consist of components of vectors that are normal to $\vec{n}$. Here, the form of Eq.(20) is used for simplicity. In the present case Eq.(20) is applied in the ξ-direction. In the η- and ζ-directions the components of (20) are permuted from the xyz-order to yzx- and zxy-orders, respectively. Furthermore, after generating the grid, the coordinate system is rotated by a small angle around every Cartesian coordinate axis, which prevents the singularity problem.

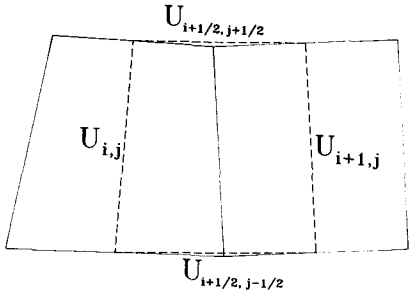

Fig. 2. Shifted control volume used for the evaluation of the viscous terms.

In order to discretize the viscous fluxes, the derivative terms must be evaluated on the cell surfaces. For the evaluation, the Gauss theorem

$$\int_V \nabla\phi dV = \int_S \phi d\vec{S} \tag{21}$$

is applied. In a two-dimensional case the volume $V_{i+1/2}$ is depicted in Fig. 2 by a dashed line. Using the Gauss theorem, the derivative of ϕ with respect to x can be expressed as

$$V(\frac{\partial\phi}{\partial x}) = \sum_{faces} S_x\phi \tag{22}$$

Similar equations hold for the y- and z-derivatives. Those values of ϕ which are not known on the surfaces of the shifted volume can be obtained as averages of the cell values. However, in a general case the derivative terms are lengthy expressions and consume a large amount of computation time. Hence in the present study a thin-layer approximation is used. In the thin-layer approximation only those terms in Eq.(22) which are evaluated in the the direction of the cell surface are retained. For example, on the surface $i+1/2, j$ of Fig. 2, the x-derivative is expressed as

$$V_{i+1/2,j}(\frac{\partial\phi}{\partial x})_{i+1/2,j} = S_{x,i+1,j}\phi_{i+1,j} - S_{x,i,j}\phi_{i,j} \tag{23}$$

Furthermore, by applying the following approximation

$$S_{x,i+1,j} \approx S_{x,i,j} \approx S_{x,i+1/2,j} \tag{24}$$

the derivative can be approximated as

$$\begin{aligned}(\frac{\partial\phi}{\partial x})_{i+1/2} &= \frac{S_{i+1/2}n_{x,i+1/2}}{V_{i+1/2}}(\phi_{i+1}-\phi_i) \\ &= \frac{n_{x,i+1/2}}{d_{i+1/2}}(\phi_{i+1}-\phi_i)\end{aligned} \tag{25}$$

Here the constant subscript j has been dropped for simplicity. In Eq.(25), $d_{i+1/2}$ approximates the distance between two neighbouring cells. By replacing the derivatives of the viscous fluxes by the formula of Eq.(25) we obtain

$$\hat{F}_{2,i+1/2} = -\frac{Ma_\infty\mu_{i+1/2}}{Re_\infty d_{i+1/2}}[(u_{i+1}-u_i)+\frac{n_{x,i+1/2}}{3}(\bar{u}_{i+1}-\bar{u}_i)] \tag{26a}$$

$$\hat{F}_{3,i+1/2} = -\frac{Ma_\infty\mu_{i+1/2}}{Re_\infty d_{i+1/2}}[(v_{i+1}-v_i)+\frac{n_{y,i+1/2}}{3}(\bar{u}_{i+1}-\bar{u}_i)] \tag{26b}$$

$$\hat{F}_{4,i+1/2} = -\frac{Ma_\infty\mu_{i+1/2}}{Re_\infty d_{i+1/2}}[(w_{i+1}-w_i)+\frac{n_{z,i+1/2}}{3}(\bar{u}_{i+1}-\bar{u}_i)] \tag{26c}$$

Here the definition of the scaled contravariant velocity component

$$\begin{aligned}\bar{u}_{i+1}-\bar{u}_i = n_{x,i+1/2}(u_{i+1}-u_i) + n_{y,i+1/2}(v_{i+1}-v_i) \\ + n_{z,i+1/2}(w_{i+1}-w_i)\end{aligned} \tag{27}$$

has been utilized.

The diffusive part of the energy flux is obtained from Eq.(18) using Eq.(25)

$$\begin{aligned}\hat{F}_{5v,i+1/2} = u_{i+1/2}\hat{F}_{2v,i+1/2} + v_{i+1/2}\hat{F}_{3v,i+1/2} + \\ w_{i+1/2}\hat{F}_{4v,i+1/2} - \frac{Ma_\infty\mu}{(\gamma-1)PrRe_\infty d_{i+1/2}}(T_{i+1}-T_i)\end{aligned} \tag{28}$$

With the present scaling of the equations, $T = c^2$, which is taken into account in the implementation of Eq.(28). Velocities and viscosity coefficients at the cell surfaces are evaluated as averages of the cell values. The form of Eqs.(26-28) is the same on all the surfaces of a computational cell. Usually the viscous terms are activated only in one or two coordinate directions. The equations have the same form in two dimensions without the contribution arising from the velocity component w.

3.2 Boundary treatment

At the free stream boundary the values of the dependent variables are kept as constants. The boundary at the wake cut is treated explicitly.

In the calculation of the convective flux at the solid boundary, the splitting is not used. By taking into account the wall boundary condition, it appears that the only contribution to the convective fluxes arises from the pressure terms in the momentum equations. A simple way to calculate the wall pressure is the following second-order extrapolation

$$p_w = \frac{3}{2}p_1 - \frac{1}{2}p_2 \tag{29}$$

Here it is assumed that the solid boundary exists below the first computational cell. As in the case of the other boundary conditions, the calculation of the wall pressure is also performed explicitly.

The calculation of the flux next to the solid boundary needs some consideration because on the other side of the cell face only one row of cells exists. For the corresponding part of the flux a simple linear interpolation is used. If the solid surface is located below the first cell, the state $U^l_{3/2}$ is calculated as

$$U^l_{3/2} = 1/2(U_1 + U_2) \tag{30}$$

This formula has a second-order accuracy which was found to be of essential importance in the calculation of lift and drag coefficients. If Eq.(30) were replaced by a first-order

formula, in many cases the resulting numerical drag would be too high relative to the physical drag.

In calculation of the viscous fluxes at the solid boundary, the central expression which appears in viscous fluxes is replaced by a one-sided formula

$$\frac{-8\phi_w + 9\phi_1 - \phi_2}{3d_w} \tag{31}$$

Here d_w is the thickness of the cell adjacent to the wall. In the calculation of the friction terms no slip boundary condition is imposed, $u_w = v_w = w_w = 0$. The heat flux on the wall is set to zero indicating an adiabatic surface. The viscosity coefficient is extrapolated on the surface as the wall pressure.

4. SOLUTION ALGORITHM

4.1 Time Integration Method

The finite-difference equations are integrated in time using the LU-factorization.[3] This is based on the approximate factorization and on the splitting of the Jacobians of the flux terms. By using the splitting and the approximate factorization, the following equations are obtained

$$(V_i + \Delta t\theta S_{i+1/2}A_i^+ - \Delta t\theta S_{i-1/2}A_i^-)\delta U_i^{**} + \Delta t\theta S_{i+1/2}A_{i+1}^-\delta U_{i+1}^{**} - \Delta t\theta S_{i-1/2}A_{i-1}^+\delta U_{i-1}^{**} = \Delta t R_i \tag{32a}$$

$$(V_j + \Delta t\theta S_{j+1/2}B_j^+ - \Delta t\theta S_{j-1/2}B_j^-)\delta U_j^{*} + \Delta t\theta S_{j+1/2}B_{j+1}^-\delta U_{j+1}^{*} - \Delta t\theta S_{j-1/2}B_{j-1}^+\delta U_{j-1}^{*} = V_j\delta U_j^{**} \tag{32b}$$

$$(V_k + \Delta t\theta S_{k+1/2}C_k^+ - \Delta t\theta S_{k-1/2}C_k^-)\delta U_k + \Delta t\theta S_{k+1/2}C_{k+1}^-\delta U_{k+1} - \Delta t\theta S_{k-1/2}C_{k-1}^+\delta U_{k-1} = V_k\delta U_k^{*} \tag{32c}$$

Again those subscripts ijk that are constant have been dropped. The superscripts $\pm$ refer to the positive and negative parts of the Jacobian matrices A, B and C. The residual R_i is defined by the right-hand side of Eq.(15). The parameter θ is chosen according to the spatial discretization; $\theta = 1.5$ is used for the second-order upwind method and $\theta = 1.33$ for the third-order upwind-biased method. In order to ensure the stability of the viscous terms the Jacobians are modified. The split Jacobians can be written as

$$A^\pm = L_\xi^{-1}(\Lambda^\pm + kI)L_\xi \qquad B^\pm = L_\eta^{-1}(\Lambda^\pm + kI)L_\eta$$
$$C^\pm = L_\zeta^{-1}(\Lambda^\pm + kI)L_\zeta \tag{33}$$

where $\Lambda^\pm$ are diagonal matrices containing the positive and negative eigenvalues of the Jacobians of the convection terms. The eigenvalues in the general coordinates are obtained from the corresponding eigenvalues in the Cartesian coordinate system by replacing the velocities by the scaled contravariant velocities. The factor k is chosen to ensure the stability

$$k = \frac{Ma_\infty \nu}{Re_\infty d\rho} \qquad \text{with} \qquad \nu = max(2\mu, \frac{\gamma\mu}{Pr}) \tag{34}$$

In Cartesian coordinates the matrices L_x, L_y and L_z and their inverses can be presented as products of two matrices which represent the transformation from the conservative to the primitive variables and from the primitive to the characteristic variables. Let for example L_x be written in Cartesian coordinates as $L_x = L_1L_2$. Then in general coordinates

$$L_\xi = L_1TL_2 \qquad L_\xi^{-1} = L_2^{-1}T^{-1}L_1^{-1} \tag{35}$$

where T is the rotation matrix given by Eq.(20). The matrices in the η- and ζ-directions are obtained similarly.

Eqs. (32) are block-tridiagonal equations and can be further simplified by applying approximate factorization. The first stage is rewritten as

$$(V_i - \Delta t\theta S_{i-1/2}A_i^-)\overline{\delta U}_i^{**} + \Delta t\theta S_{i+1/2}A_{i+1}^-\overline{\delta U}_{i+1}^{**} = \Delta t R_i \tag{36a}$$

$$(V_i + \Delta t\theta S_{i+1/2}A_i^+)\delta U_i^{**} - \Delta t\theta S_{i-1/2}A_{i-1}^+\delta U_{i-1}^{**} = V_i\overline{\delta U}_i^{**} \tag{36b}$$

Similar equations can be written for the η- and ζ-directions. These equations have a block-bidiagonal structure and can be inverted using a similar technique to that with the MacCormack method.[4] Thus the implicit stage consists of a backward and forward sweep in every coordinate direction. These sweeps are effectively explicit. Presently, the starting values of the implicit sweeps at the lower and upper boundaries are simply set to zero.

It should be noted that the splitting is based on the Jacobians which are not the true Jacobians of the fluxes (16). Firstly, the splitting of the convection terms is based on the splitting of Steger and Warming[5] instead of the splitting of Van Leer. Secondly, the linearization of the viscous terms is simplified. Because the mass equation does not contain any diffusion term, in the simplified treatment of the viscous effects a smoothing term is implicitly added on the left-hand side of Eq.(32). The amount of this smoothing depends on the time-step.

In the present calculations only the steady state is of interest, hence a spatially varying time step has been applied. Because the true Jacobians are not used, the time-step size is limited. However, the computation time of the bidiagonal equation system is considerably less than the computation time of the block tridiagonal system arising from the linearization of the fluxes (15). Furthermore, it appears that the implicit stage has good smoothing properties and, consequently, its effectiveness can be considerably enhanced combining it with a multigrid.

4.2 Multigrid Method

In order to make the method more efficient, a multigrid cycling is applied. In the following, h_i denotes the grid level, h_1 being the finest level.

The algorithm follows the method of Jameson[6]:

1) Calculate the residual R_{h_1} on the finest grid. The residual is defined by the right-hand side of Eq.(15).

2) Perform the implicit phase and update the solution.

The following steps 3-9 are repeated until the coarsest grid level is reached:

3) Recalculate the residual $R_{h_{i-1}}$ on the previous grid level.

4) Calculate a new residual using the forcing function $P_{h_{i-1}}$

$$R^*_{h_{i-1}} = R_{h_{i-1}} + P_{h_{i-1}} \tag{37}$$

On the second grid level no forcing function from the finest level exists. Thus $R^*_{h_{i-1}}$ is simply replaced by the residual calculated in the third step.

5) Transfer the residual of Eq.(37) and the variables from grid h_{i-1} to the next coarser grid h_i. The transfer of the variables is performed as

$$U^t_{h_i} = \sum V_{h_{i-1}} U_{h_{i-1}} / V_{h_i} \tag{38}$$

and the transfer of the residual as

$$R^t_{h_i} = \sum R^*_{h_{i-1}} \tag{39}$$

The sum is taken over the cells which approximately occupy the cell on the coarse grid.

6) Calculate the residual R_{h_i} using the transferred values of Eq.(38).

7) Calculate the forcing function from

$$P_{h_i} = R^t_{h_i} - R_{h_i} \tag{40}$$

8) Recalculate the residual from

$$R^*_{h_i} = R_{h_i} + P_{h_i} \tag{41}$$

In the present case only one iteration cycle per grid level is performed. Then actually $R^*_{h_i}$ is the same as the residual transferred via Eq.(39).

9) Perform the implicit phase using $R^*_{h_i}$ as a residual and update the solution U_{h_i} on grid h_i.

It is essential to use larger time steps on the coarse grid levels than on the fine levels. As in practice there is a stability limit with the present time integration method, a certain value of CFL cannot be exceeded. However, it is possible to apply the same Courant number on every grid level, this leading to a large time step on the coarse grid levels. Furthermore, it is possible to use the first-order method in the calculation of fluxes on the coarse grids. Since the solution on the coarse grids is determined by the residuals on the finest grid, the final solution does not depend on the spatial accuracy on the coarse grids. This treatment will save some computation time and provide a means to further accelerate the convergence rate. This is due to the fact that when a first-order method is used, the time integration is stable with longer time steps than in the case of the second-order method. Hence it is possible to use a larger value of CFL number on the coarse grid levels than on the finest level where an accurate solution is desired. Generally this will speed up the convergence.

When the coarsest grid is reached, the corrections are transferred back to the finer levels. Let $U^+_{h_{i+1}}$ be the final value of $U_{h_{i+1}}$ resulting from both the correction calculated on grid h_{i+1} and the correction transferred from grid h_{i+2}. Then

$$U^+_{h_i} = U_{h_i} + I^{h_i}_{h_{i+1}} (U^+_{h_{i+1}} - U^t_{h_{i+1}}) \tag{42}$$

Here the interpolation operator $I^{h_i}_{h_{i+1}}$ is simply a direct transfer of the difference $U^+_{h_{i+1}} - U^t_{h_{i+1}}$ from the coarse grid cell to the appropriate eight (or four in a two-dimensional case) fine grid cells.

The calculation on the coarse grid levels is performed in exactly the same way as on the finest grid level. The only exception is the first-order interpolation on the coarse grids. This similarity allows us to use the same subroutines on each level by passing the arrays through the parameter lists.

5. RESULTS

5.1 Inviscid 2-dimensional flow

As an inviscid test case we consider a transonic flow over an NACA 0012 airfoil. The test case is at $Ma = 0.85$ and $\alpha = 1°$. In this study an O-type algebraically generated grid is used. The grid size is 128×32 and five grid levels (the finest grid and four coarse grid levels) are utilized in the calculations. The resulting pressure coefficient and the Mach contours are shown in Figs. 3 and 4. The calculated force coefficients are $c_d = 0.00579$ and $c_l = 0.350$, which agree well with the values found in the literature.[7] In this calculation a second-order extrapolation with the limiter of Van Albada et al.[8] is used for U^l and U^r in both coordinate directions. The limiter may have some effect on the calculated force coefficients. In transonic cases this effect is usually negligible, but in subsonic cases the limiter produces a relatively large numerical drag. If no shocks are present, the calculation should be performed with a third-order upwind-biased interpolation without limitation, which then leads to a reasonable drag value.

The convergence histories with different numbers of grid levels are shown in Fig. 5. The Courant numbers in the computations were 2.5 on the finest level and 4.0 on the coarse levels. The first-order method used on the coarse levels allows to use somewhat larger values for the CFL-number on those levels. Since the computations were performed with 64-bit arithmetic, from Fig. 5a it is seen that in this particular case the computation ceases to converge before the machine accuracy is obtained. This does not matter because for practical purposes the result is accurate enough when the maximum change in density is about 1×10^{-5}. The machine accuracy can be obtained e.g.

by reducing the CFL-numbers. The effect of a larger coarse grid CFL-number on the convergence is shown in Fig. 5b and on the convergence of the lift on Fig. 5c. The optimum choice of CFL-numbers with a second-order method is about 4.0 on the fine grid level and 6.0 on the coarse grid levels. Although not shown, these CFL-numbers will accelerate the convergence so that in the present case the residual of 1×10^{-5} is reached in fewer than 150 cycles.

5.2 Viscous 2-dimensional flow

As an example of the viscous simulations a case of a turbulent flow over an NACA 0012 airfoil is introduced. Results concerning laminar flow are provided in Ref. 12. The flow conditions are $Ma = 0.7$, $Re = 9.0 \times 10^6$ and $\alpha = 1.49°$. In the case of a turbulent flow the viscosity and the heat conductivity are replaced by

$$\mu + \mu_t, \qquad \frac{\mu}{Pr} + \frac{\mu_t}{Pr_t} \tag{43}$$

where μ_t is the turbulent viscosity. For the turbulent Prandtl number Pr_t, a constant value of 0.9 has been specified. The turbulent viscosity is evaluted using the Baldwin-Lomax turbulence model.[9]

The grid size is 192×64 and the grid is of a C-type. The minimum cell thickness is 5×10^{-5} at the leading edge, increasing to 2.5×10^{-4} at the trailing edge. The computed pressure coefficient together with the experimental results[10] are shown in Fig. 6 and the computed Mach contours in Fig. 7. For the surface pressure the agreement between the experimental data and computation is good. The computed force coefficients are $c_d = 0.00803$ and $c_l = 0.247$, which are close to the values $c_d = 0.0079$ and $c_l = 0.241$ determined experimentally and well within the limits of other computations.[11] In the calculation the third-order interpolation method was used. The limiter would increase the calculated drag value.

The computation time with the Cray X-MP/432 computer is 27μs per volume and grid point with a single grid. With three grid levels the method requires 55μs and with five levels 56μs. These values are for the third-order interpolation method without the limiter. If the limiter were included, the execution times would be longer by about 10 %. The laminar calculation would reduce the computation times by about 15 %.

The iteration histories are shown in Fig. 8. Owing to the larger number of grid points and the concentration of grid points inside the boundary layer, the computation requires many more iteration cycles than the inviscid case. In the present case the application of five grid levels is possible. It has been found that sometimes the viscous calculation has to be performed by using only three or four grid levels. The use of more grid levels in those cases would result in an oscillatory solution.

5.3 Supersonic Flow over a Body of Revolution

In order to demonstrate the method's ability to resolve complex flow phenomena, supersonic flow over a body of revolution at high angles of attack has been simulated. The flow patterns that a body experiences as it is pitched from 0° to 90° angle of attack are discussed in Ref. 13. At moderate angles of attack ($\alpha \approx 10°$), the crossflow about the body begins to separate over the leeside generating symmetrical, counter-rotating vortices on the leeside. At large incidences and depending on a number of other factors, the vortices over the leeside may become asymmetric. Finally, at high angles of attack ($\alpha \approx 60°$) an unsteady wake-like flow is obtained.

The purpose of the present calculations was to validate the code in 3-D by providing solutions which agree qualitatively with the experiments and results obtained elsewhere.[13] With a zero angle of attack the calculations could also be checked with the aid of an axisymmetric code. In order to calculate this type of turbulent flow the standard Baldwin-Lomax turbulence model has to be modified. The justification for the use of an algebraic turbulence model and the necessary modifications are discussed in Ref. 14. In the following, these modifications are briefly summarized.

The major difficulty encountered in applying the Baldwin-Lomax turbulence model to bodies with crossflow separation is that of properly evaluating the scale length y_{max}. This is because the function $F(y)$ of the standard Baldwin-Lomax model shows multiple maxima in the regions of separation. The standard model would use the largest maximum for F_{max}, which leads to much too high a value for the turbulent viscosity. This is avoided when the maximum is considered to have been found when the value of $F(y)$ drops to 90% of the local maximum value. Choice of F_{max} in this way should exclude the second, spurious maximum. The value of 90% has been used in this study according to Ref. 14. However, it seems that sometimes the first maximum is very flat and would not be detected with the 90% criterion. A further test is applied. The computation proceeds in a circumferential direction around the body. On each ray a cut-off distance is specified in terms of y_{max} from the previous ray as $y_{cutoff} = 1.5 y_{max}$. If no maximum in $F(y)$ is found along the ray for $y \leq y_{cutoff}$, the values of F_{max} and y_{max} are taken as those found on the previous ray. In this way a physically reasonable value for μ_t will be chosen for those rays close to the crossflow separation points.[14]

The blunt-nose cylinder used in the calculations is the same as in Ref. 13 (Fig. 9). The grid sized $80 \times 64 \times 48$ was generated by rotating a two-dimensional grid around the axis of symmetry. The two-dimensional grid was generated by a transfinite interpolation method. The grid is highly clustered in the radial direction. About 30 of the 64 points in the radial direction are placed inside the boundary layer. The minimum cell thickness near the nose is 3.5×10^{-5}, increasing to 1.8×10^{-4} at the base. In the circumferential direction the radial clustering is constant. The use of only 48 cells in the circumferential direction results in a circumferential spacing of 7.5°.

The free stream conditions of the test cases are as follows:

$$Ma = 1.6, \qquad Re_D = 5 \times 10^5$$

Both turbulent and laminar simulations have been made at three angles of attack.

Laminar Flow at $\alpha = 20°$. As in Ref. 13, no attempt was made to decide whether the flow is laminar, transitional or fully turbulent. Instead, all the cases were calculated as if the flow were either laminar or fully turbulent. At $\alpha = 20°$ the laminar longitudinal pressure distributions are shown in Fig. 10 together with the experimental data. Our results agree well with the results obtained elsewhere[13], but the agreement with experimental results is not particularly good at circumferential positions of $\zeta = 90°$ and $\zeta = 180°$. The calculated normal force coefficient C_N is 2.08, while the experimental result is 1.92.[13] The base is used as the reference area.

Two axial stations are used to show the crossflow density contours. Stations I and II (Fig. 9) are located immediately after the forebody-cylinder junction ($x/D = 3.17$) and upstream of the base ($x/D = 6.17$). Comparison of these results shows how the primary vortex grows towards the base (Figs. 11a and 12a). The circumferential skin friction coefficient is plotted on Fig. 13. The primary separation takes place at $\zeta = 106°$ and the primary reattachment point is located at $\zeta = 0°$. The same locations were obtained in the calculations of Ref. 13. The secondary separation occurs at $\zeta = 34°$ and the secondary reattachment point is at $\zeta = 71°$. The reference results are 27° and 81°, respectively. The reason for this deviation lies obviously in the inadequate mesh spacing in the circumferential direction. The present mesh spacing is 7.5°, while a spacing of 2.5° is required for accurate results.[14] According to the computations[14] the secondary separation point moves towards the windward side and the secondary reattachment point moves towards the leeward side as the mesh spacing is increased. This behaviour is also seen in the present calculations.

Turbulent Flow at $\alpha = 20°$. In this case the longitudinal pressure distribution differs significantly from the laminar result only at the position $\zeta = 90°$ (Fig. 10). The difference in the crossflow density contours at Station I is also small (Fig. 11b). At Station II the deviation is more pronounced (Fig. 12b). At $\zeta = 90°$ there is a strong crossflow shock. In the present calculation the shock profile is smeared, which is again caused by the coarse mesh spacing in this direction. However, the results agree qualitatively with the results of Ref. 13. The largest difference between the present results and those of Ref. 13 is the existence of the primary vortex at Station I in our results. In Ref. 13 the primary vortex at this station is visible only in the laminar result.

In the turbulent calculation we obtain $C_N = 1.94$, which is very close to the experimental value 1.92. The primary separation at Station II occurs at $\zeta = 92°$ (in Ref. 13 they also found 92°). The secondary separation takes place at $\zeta = 31°$ (31°) and the secondary reattachment at $\zeta = 58°$ (51°).

Laminar and Turbulent Flow at $\alpha = 32°$. In this case the differences between the laminar and turbulent calculations are smaller than in the previous case. In the laminar case the normal force coefficient C_N is 4.31. Assuming turbulent flow, we obtain $C_N = 4.29$. These values are reasonably close to the experimental value 4.19.[13] Although not shown, the longitudinal turbulent and laminar pressure distributions could not be distinguished from each other. The agreement between the calculated and measured pressures is better than at $\alpha = 20°$ (Fig. 14). Since the difference in the laminar and turbulent crossflow density contours is small, only the laminar results are shown (Figs. 15 and 16). The shock surface on the windward side is visible at Station I. The circumferential friction coefficient is depicted in Fig. 17. In the laminar case the primary separation occurs at $\zeta = 84°$ (in Ref. 13 they found 86°). Before the separation the turbulent friction is significantly larger than the laminar friction. On the separation region the difference between the laminar and turbulent friction coefficients is small. The secondary separation occurs at $\zeta = 28°$ (25°) and the secondary reattachment point is at $\zeta = 51°$ (52°).

Laminar and Turbulent Flow at $\alpha = 44°$. The longitudinal pressure coefficient distributions of the laminar computation are given in Fig. 14. Again the agreement with the experimental data is good. The force coefficient is 6.61 and in the turbulent case we obtain about 6.62. The laminar result is within 4% of its experimental value (6.38). The crossflow density contours at Station II are given in Fig. 18. It is seen that the flow is practically symmetrical in the laminar case, whereas in the turbulent case an asymmetric nonsteady flow is obtained. At Station I the flow is steady. On the surface the unsteady behaviour is visible on a small area in the range $-60° \leq \zeta \leq 60°$, i.e. where the secondary separation occurs, its effect on the normal force coefficient only being about 0.2 %. The circumferential skin friction coefficient is shown in Fig. 19. In the laminar case the primary separation occurs at $\zeta = 71°$ (in Ref. 13 $\zeta = 81°$). The secondary separation occurs at $\zeta = 24°$ (22°) and the secondary reattachment point is at $\zeta = 41°$ (48°).

Code performance In this application the maximum Courant number must be significantly decreased from that used in the airfoil calculations. In the calculations performed a Courant number of 0.5 was applied. The same reduction in the maximum allowable Courant number also takes place in two-dimensional axisymmetric calculations. Furthermore, it is difficult to get started utilizing the grid size of $80 \times 64 \times 48$. For example, the turbulent simulation at $\alpha = 20°$ was started by calculating firstly 100 cycles using a first-order interpolation method with a single grid level. The next 100 cycles were calculated with a second-order method and the limiter. From 200 to 500 cycles two grid levels were applied and finally after 500 cycles five levels were in use. After 500 cycles the limiter was on in the axial direction only. In the circumferential direction the second-order method was used and in the radial direction the third-order method. In spite of the gradual start, the convergence of a turbulent calculation is fast at $\alpha = 20°$ and $\alpha = 32°$. The lift and drag coefficients are practically constants after 700 cycles (Fig. 20). Since there are no difficulties in beginning the calculation with a coarser grid, the efficiency of the calculation could be significantly increased by initializating the calculation by mesh sequencing.[13]

The behaviour of the laminar calculation is different. It appears that although practically steady flow is established along the body, an unstable flow is developed behind the base. The same phenomenon is also present in axisymmetric simulations. The density histories at $\alpha = 0°$ are monitored in Fig. 21. The densities are on the outer edge of the boundary layer: the first one is between Stations I and II, the second one a little behind the base. The density in the body region is finally constant whereas time-dependent flow is established in the wake region.

At the highest angle of attack (44°) an usteady flow is also established assuming turbulent conditions. The unsteadiness is much more severe than in the laminar computations and occurs also in the body region. The resulting density contours at Station II reveal an asymmetric time-dependent vortex structure. In spite of the time-dependent behaviour, the computed normal force coefficient is almost constant.

The computation time of a single-grid calculation with the turbulence model is around $37\mu s$ per grid point and cycle. With five grid levels the computation time is about $74\mu s$ with the Cray -XMP/432.

6. CONCLUSIONS

A numerical method for compressible flow equations which utilizes multigrid acceleration for the convergence has been presented. The method is suitable for inviscid and viscous flow problems. The discretization is performed with the aid of a finite-volume formulation. The convective fluxes are calculated using Van Leer's splitting, while for the viscous fluxes the thin-layer approximation is applied. The time integration is performed employing a simplified implicit scheme which results in a limited CFL-number. The convergence is accelerated using a multigrid method.

The method has been applied for inviscid and viscous simulations over an NACA 0012 airfoil. The calculated force coefficients are in reasonable agreement with experiments and other calculations. At least a threefold saving in computing time is obtained by applying the multigrid acceleration. Especially the convergence of the lift coefficient is enhanced.

In three dimensions the method has been applied for a simulation of a supersonic flow over a body of revolution. The results generally agree with those obtained elsewhere and also with experimental data. Owing to the coarse mesh spacing in the circumferential direction, the secondary separation is modelled inaccurately, but the primary flow features are well predicted.

REFERENCES

1. Van Leer, B., Flux-Vector Splitting for the Euler Equations, Proc. 8th Int. Conf. on Numerical Methods in Fluid Dynamics, Aachen, 1982 (also Lecture Notes in Physics, Vol. 170, 1982).

2. Roe, P.L., Characteristic-Based Schemes for the Euler Equations, Annual Review of Fluid Mechanics, 1986.

3. Obayashi, S., Kuwahara, K., An Approximate LU Factorization Method for the Compressible Navier-Stokes Equations, J. Comput. Phys., Vol. 63, No. 1, March 1986.

4. MacCormack, R.W., A Numerical Method for Solving the Equations of Compressible Viscous Flow, AIAA Journal, Vol. 16, No. 9, Sept. 1982.

5. Steger, J.L., Warming, R.F., Flux-Vector Splitting of the Inviscid Gasdynamic Equations with Application to Finite Difference Methods, J. Comput. Phys., Vol.40, No. 2, April 1981.

6. Jameson, A., Yoon, S., Multigrid Solution of the Euler Equations Using Implicit Schemes, AIAA Journal, Vol. 24, No.11, Nov. 1986.

7. Dervieux, A., et al. Report on the GAMM Workshop on Numerical Simulation of Compressible Euler Flows, in Notes on Numerical Fluid Mechanics, Vol. 20, Friedr. Vieweg & Sohn, Braunschweig 1988.

8. Van Albada, G.D., Van Leer, B., Roberts, W.W. Jr., A Comparative Study of Computational Methods in Cosmic Gas Dynamics, Astronomy and Astrophy., Vol. 108, No. 76, 1982.

9. Baldwin, B.S., Lomax, H., Thin Layer Approximation and Algebraic Model for Separated Turbulent Flows, AIAA Paper 78-257, Jan. 1978.

10. Harris, C.D., Two-Dimensional Aerodynamic Characteristics of the NACA 0012 Airfoil in the Langley 8-Foot Transonic Pressure Tunnel, NASA TM-81927, 1981.

11. Holst, T.L., Viscous Transonic Airfoil Workshop Compendium of Results, J. Aircraft, Vol. 25, No. 12, Dec. 1988.

12. Siikonen, T., Hoffren, J., Solution of the Thin-Layer Navier-Stokes Equations for Laminar Transonic Flow, Helsinki University of Technology, Laboratory of Aerodynamics, Report No. A-11, 1989.

13. Baysal, O., Fouladi, K., Miller, D.S., Computations of Supersonic Flows Over a Body at High Angles of Attack, AIAA Journal, Vol. 27, No. 4, April 1989.

14. Degani, D., Schiff, L.B., Computation of Turbulent Supersonic Flows around Pointed Bodies Having Crossflow Separation, J. Comput. Phys., Vol. 66, No. 1, Sept. 1986.

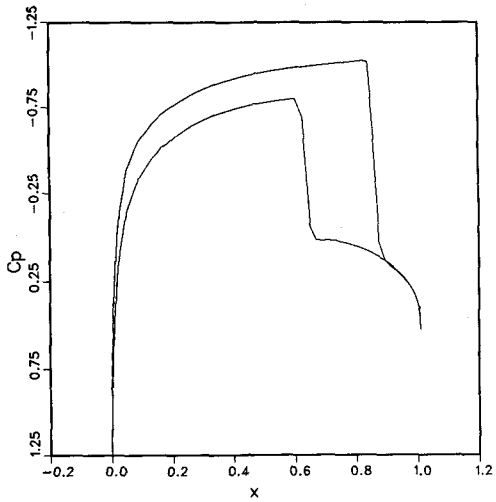

Fig. 3. Pressure coefficient distribution for the NACA 0012 airfoil at $Ma = 0.85$, $\alpha = 1°$.

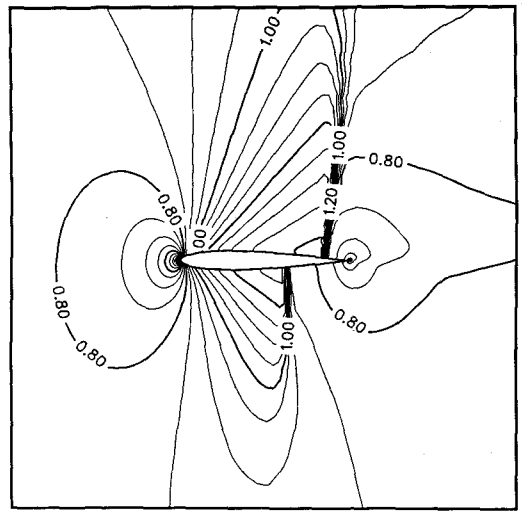

Fig. 4. Mach contours for the NACA 0012 airfoil at $Ma = 0.85$, $\alpha = 1°$.

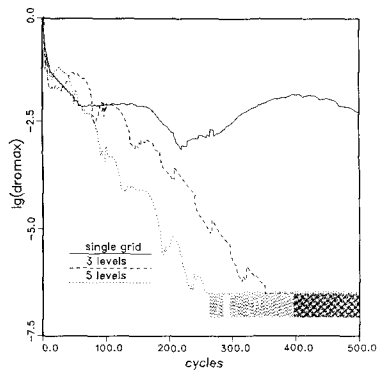

Fig. 5a. Convergence of the maximum change in density applying different numbers of grid levels.

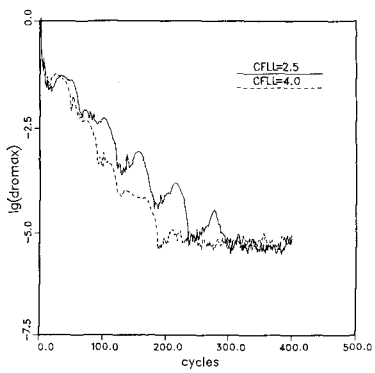

Fig. 5b. The same applying either a constant or a variable Courant number with five grid levels.

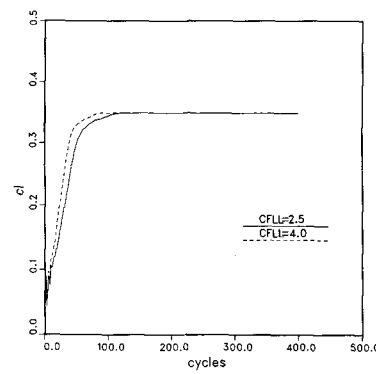

Fig. 5c. Convergence of the lift with a constant or a variable Courant number.

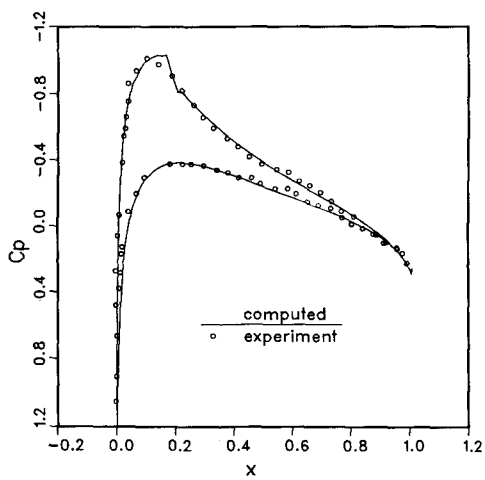

Fig. 6. The calculated and experimental pressure coefficients at $Ma = 0.7$, $Re = 9 \times 10^6$, $\alpha = 1.49°$.

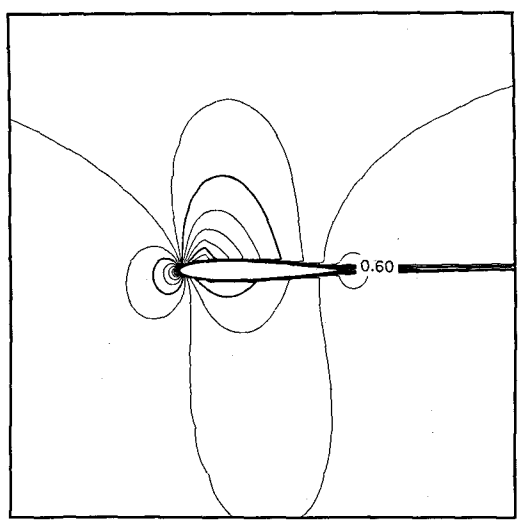

Fig. 7. Mach contours at $Ma = 0.7$, $Re = 9 \times 10^6$, $\alpha = 1.49°$.

a)

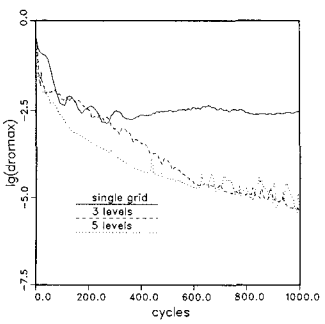

b)

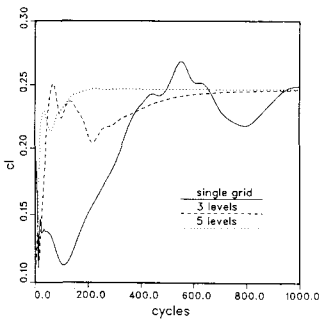

Fig. 8. Convergence of a) maximum change in density, b) lift at $Ma = 0.7$, $Re = 9 \times 10^6$, $\alpha = 1.49°$.

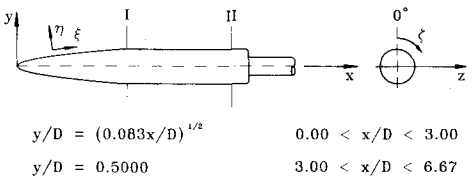

Fig. 9. The scheme of the blunt-nose cylinder.

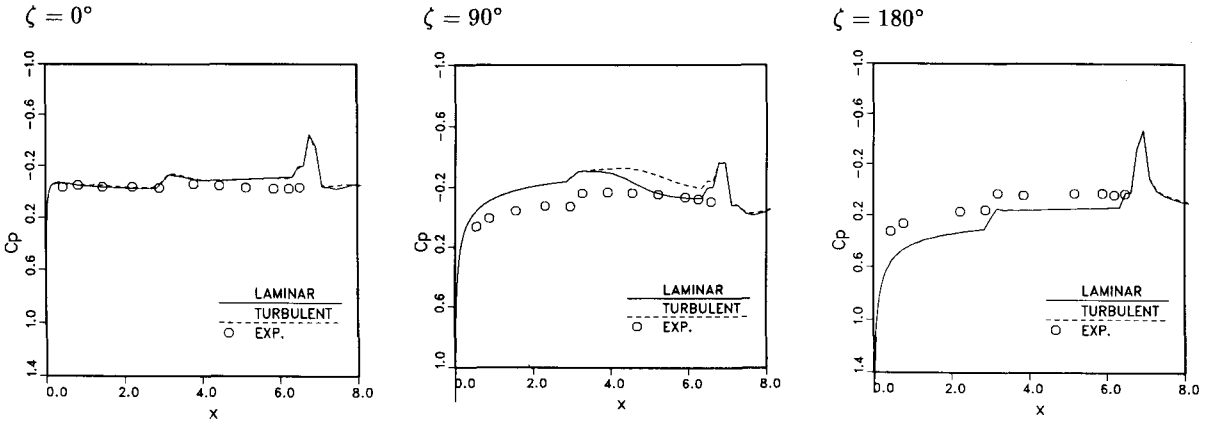

Fig. 10. Longitudinal pressure coefficient distributions of laminar and turbulent flows at $\alpha = 20°$.

a)

b)

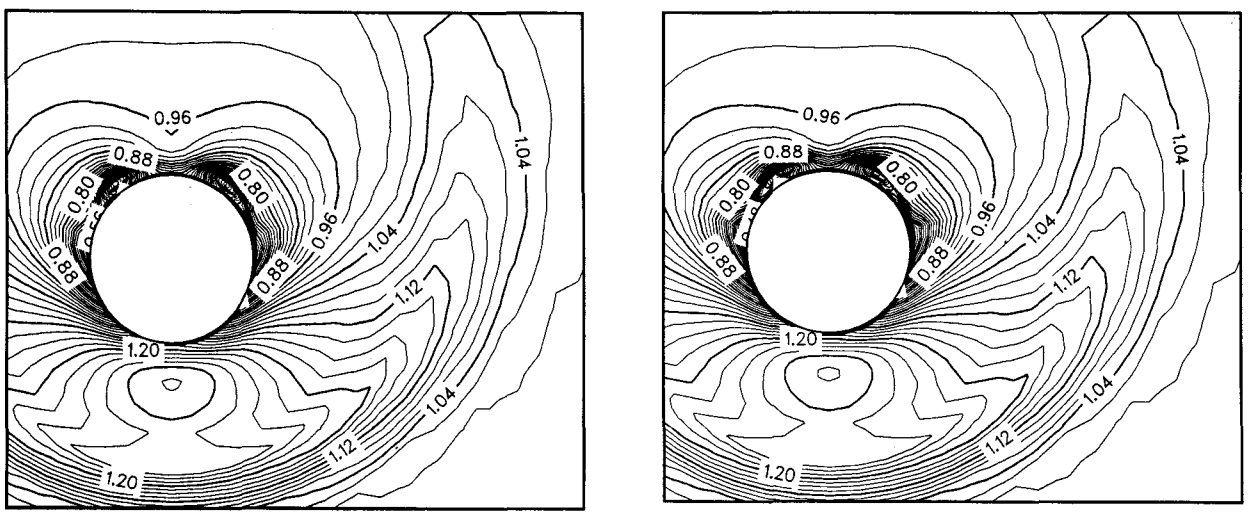

Fig. 11. Crossflow density contours for a) laminar and b) turbulent flow at Station I for $\alpha = 20°$.

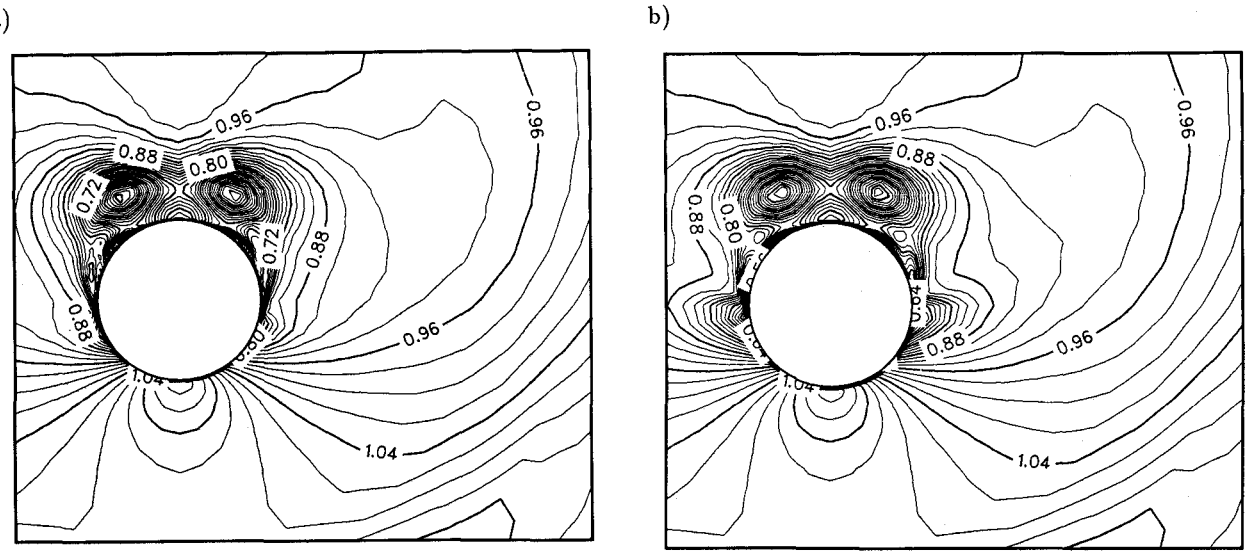

Fig. 12. Crossflow density contours for a) laminar and b) turbulent flow at Station II for $\alpha = 20°$.

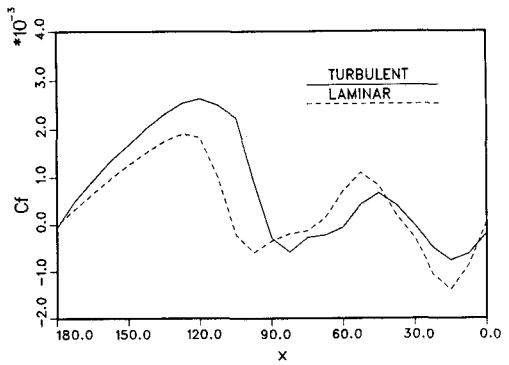

Fig. 13. Circumferential skin friction coefficient at Station II for $\alpha = 20°$.

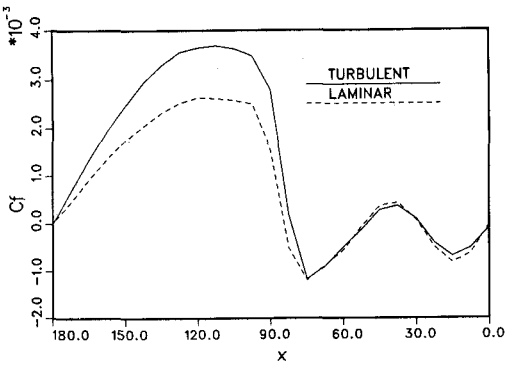

Fig. 17. Circumferential skin friction coefficient at Station II for $\alpha = 32°$.

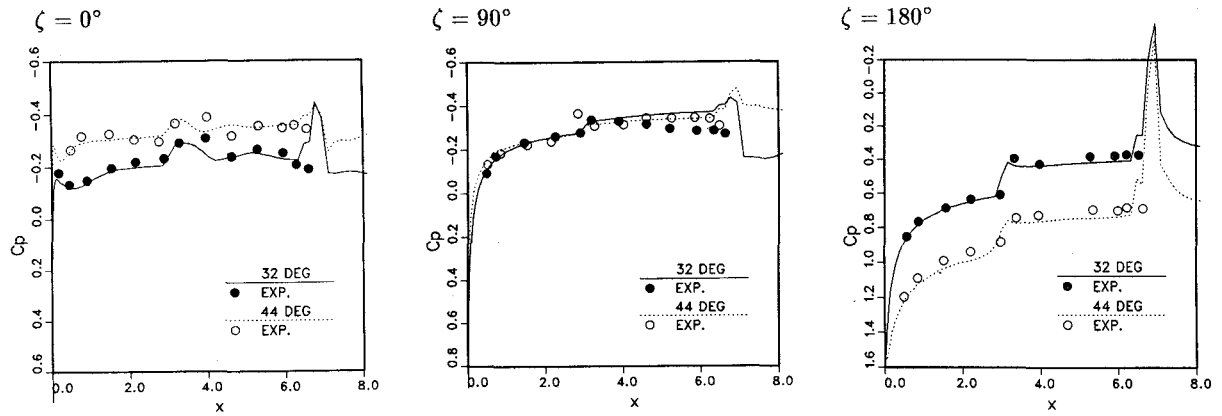

Fig. 14. Longitudinal pressure coefficient distributions of a laminar flow at $\alpha = 32°$ and $\alpha = 44°$.

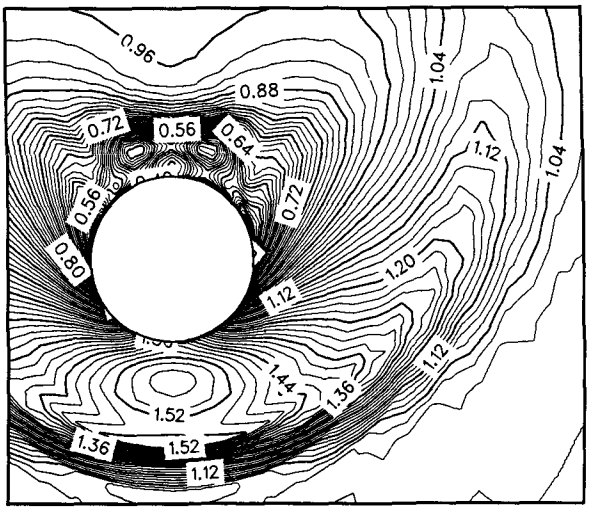

Fig. 15. Crossflow density contours for a laminar flow at Station I for $\alpha = 32°$.

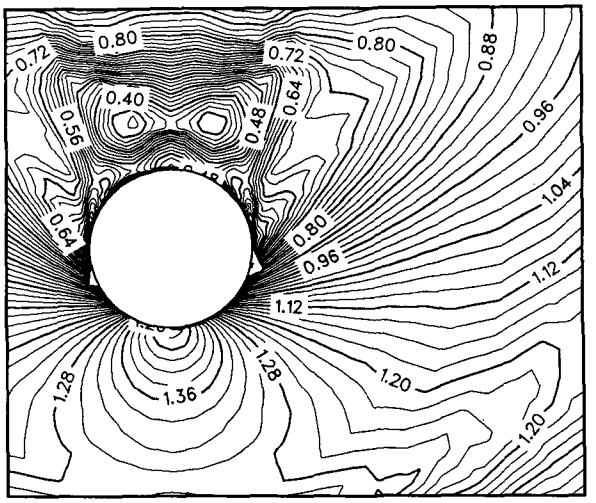

Fig. 16. Crossflow density contours for a laminar flow at Station II for $\alpha = 32°$.

a)

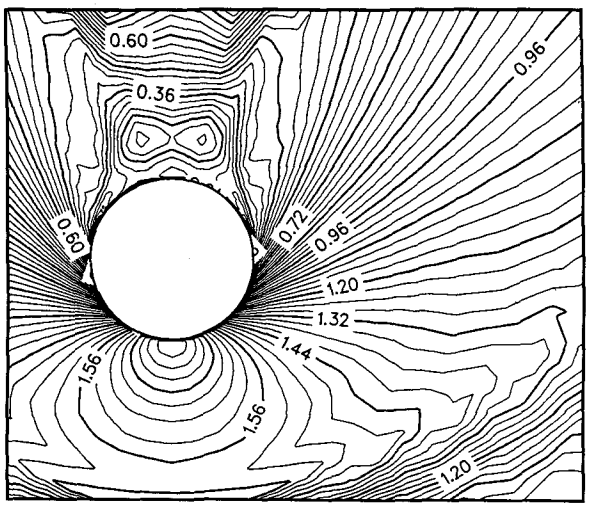

b)

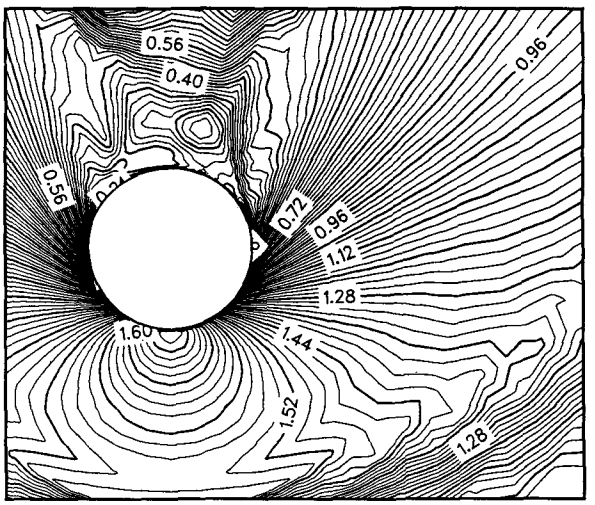

Fig. 18. Crossflow density contours for a) laminar and b) turbulent flow at Station II for $\alpha = 44°$.

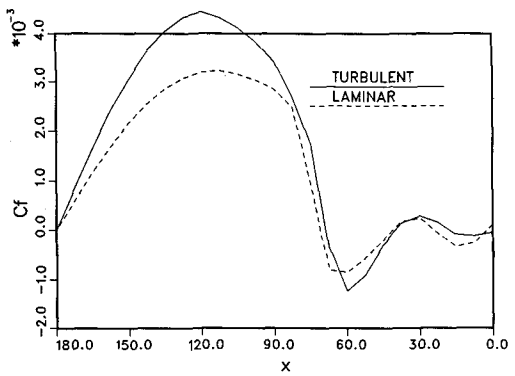

Fig. 19. Circumferential skin friction coefficient at Station II for $\alpha = 44°$.

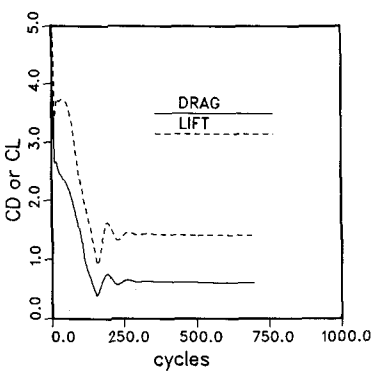

Fig. 20. Convergence of the drag and the lift for $\alpha = 20°$ using a reference area equal to D^2.

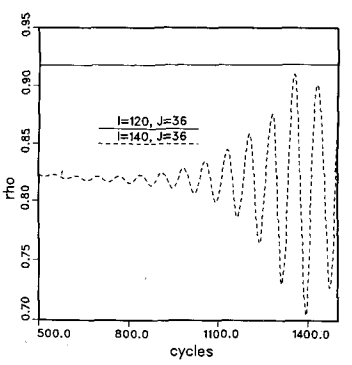

Fig. 21. Density histories near the surface of the body (I = 120) and immediately behind the base (I = 140).